Power Electronics and Drives
Volume 11(46), 2026 DOI: 10.2478/pead-2026-0014

A Comparative Study of Control Schemes Based on PI Controllers and State-Feedback Control for Grid-Connected Converters

Research paper

Marek Michalczuk

Department of Electrical Drive Division, Warsaw University of Technology, Institute of Control and Industrial Electronics, Warsaw, Poland

Received: 28 January, 2026; Received in the revised form: 31 March, 2026; Accepted: 28 April, 2026

Abstract: This paper provides a comparative analysis of two classical control strategies applied to a grid-connected voltage-source converter (VSC) with an L-type filter. The first method employs a cascade control structure with proportional–integral controllers, while the second uses a full-state feedback controller designed via the linear quadratic regulator method. A linearised state-space model of the converter, including controller and modulation delays, is developed and consistently used for both control schemes to enable a fair comparison. The control approaches are evaluated through detailed numerical simulations under identical operating conditions, including grid voltage disturbances, load changes and reference variations. Performance is assessed based on transient response, disturbance rejection, control effort, robustness to parameter changes and stability margins. Disk margin (DM) analysis offers a conservative, comprehensive evaluation of closed-loop stability. The results show that, although both strategies attain similar settling times, the full-state feedback controller offers superior disturbance rejection, reduced peak currents and notably larger stability margins. The paper aims to provide practical insights and guidelines for selecting suitable control strategies for power electronic systems.

Keywords: *grid-connected converter • full state feedback • stability analysis • voltage-oriented control*

1. Introduction

The ongoing development of renewable energy sources and distributed generation has led to widespread deployment of power electronic grid-connected converters (GCCs). Due to the widespread use of systems such as photovoltaic systems, wind turbines and energy storage systems, the design of robust and high-performance control strategies for GCCs is an active area of research (Dmitruk, 2024; Galecki and Kaszewski, 2025a; Iwański et al., 2023; Iwanski et al., 2021; Iwaszkiewicz et al., 2025; Krystkowiak and Gwóźdź, 2018; Kulikowski and Sikorski, 2016; Peykarporsan et al., 2025). This paper focuses on two classical voltage oriented control (VOC) methods, the first based on a cascade structure of PI controllers (Iwanski et al., 2016; Liu et al., 2025; Piasecki et al., 2012; Tian et al., 2025a; Ufnalski et al., 2022) and the second using a state feedback controller (Busada et al., 2015; Michalczuk et al., 2023; Rahman et al., 2020; Tian et al., 2025b). Despite the extensive use of both control strategies, a comprehensive and fair comparison between PI cascade control and state feedback control for GCCs remains essential. The core contribution of this paper is to provide a fair, multi-criteria comparison of two well-established control strategies, highlighting their relative strengths and weaknesses under consistent conditions.

Often, engineers' choices for control architectures are based on subjective preferences and prior experience rather than on the actual qualitative differences among individual control methods. System designers frequently use general arguments about the properties of certain control architectures (Åström and Murray, 2021; Franklin et al., 2002), but these characteristics are not necessarily relevant to a specific application. For example, when comparing PI controllers with state feedback controllers, one might highlight the PI-based structure's inferior ability to decouple

* *Email: marek.michalczuk@pw.edu.pl*

control paths or limit the mutual influence of state variables. However, in the case of GCC, this argument is largely unfounded, as we can easily design an effective decoupling network, as will be discussed in the third section of this publication. Conversely, the common belief that a state controller is a complex structure requiring high computational effort to estimate the state vector is often false, since a practical implementation of a state controller relies on the same measurement signals as a system with PI controllers and does not need additional calculations of the plant model to determine the state vector. Therefore, in this publication, both control methods will be presented in detail and qualitatively compared.

When conducting a comparative analysis of two control structures, it is essential to consider not only qualitative performance indicators related to system response but also stability and robustness. The selection of controller gains is inherently a trade-off between the desired dynamic performance and the stability of the closed-loop system. Therefore, control systems should not be compared based on a single evaluation criterion. In particular, focusing solely on the dynamic response may lead to incomplete or even misleading conclusions, as similar performance indices can be achieved by different control structures while exhibiting significantly different stability margins. In this context, the present paper provides a comprehensive comparison of the considered control structures, accounting for both dynamic performance and stability- and robustness-related metrics, to deliver a balanced and reliable assessment.

The following section presents the mathematical model of the GCC. The complete design procedures for PI controllers and the state-feedback controller are described and compared in Section 3. Then, Section 4 presents simulation results for both control structures, along with a comparative analysis, including stability assessments for each system. The publication will be summarised in Section 5, where challenges faced in implementing these structures will be discussed, and in Section 6, where conclusions will be drawn.

2. Grid Connected Converter

This section describes the system modelling and the control system design procedure. The physical plant comprises a voltage-source converter (VSC) connected to the grid via an L-type filter (Figure 1). As shown, v_d, v_q are the AC side grid voltage, v_d^{cnv} and v_q^{cnv} are the converter side voltage represented in a d-q frame oriented with the grid voltage space sector. R-L components represent the resistance and inductance of the grid side filter. i_{load} is the load current flowing from the DC bus of the GCC. u_d, u_q and u_α, u_β are control signals, in rotating and stationary frames, respectively, representing the commanded converter output voltage from the control system. Because the control algorithms are implemented in a rotating reference frame, the AC phase current signals are also transformed into i_d and i_q components. In the considered control schemes, which operate as a grid-following strategy, synchronisation with the grid is achieved using a phase-locked loop (PLL). In the event of grid frequency deviations, the PLL adjusts the estimated angular frequency to maintain synchronisation, resulting in a transient phase error i.e., compensated by its internal PI controller (Guo et al., 2011; Sun et al., 2026; Zhao et al., 2021). Consequently, the rotating reference frame adapts to the grid frequency. The PLL dynamics have been neglected in the presented analysis. While PLL dynamics may influence the system response to some extent, they are not critical to the comparative nature of this study. The selected system parameters used in the simulation studies are summarised in Table 1.

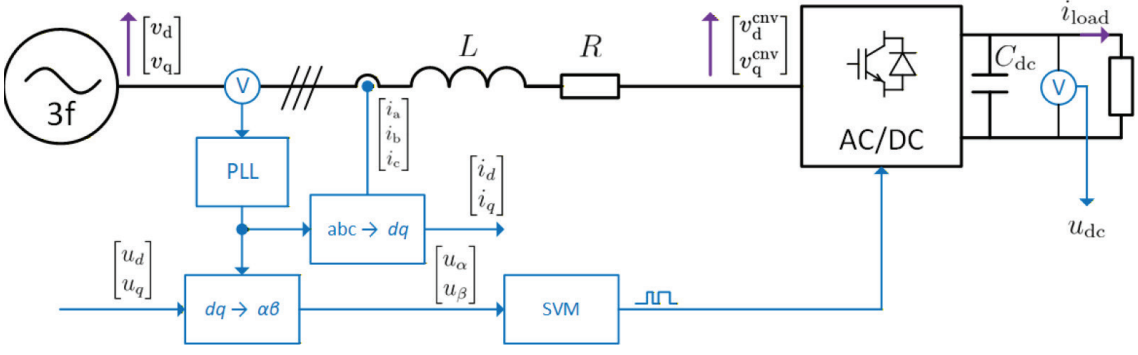

Figure 1. Block diagram of the plant. PLL, phase-locked loop.

Table 1. Parameters of grid GCC.

Parameter name	Symbol	Value
Nominal grid voltage (RMS)	V_n	400 V
Nominal grid current (RMS)	I_n	14 A
Nominal grid frequency	f_n	50 Hz
Input filter inductance	L	2 mH
Input filter resistance	R	0.1 Ω
DC-link capacitance	C_{dc}	500 μF
Switching/sampling frequency	f_{sw}	10 kHz
Nominal DC voltage	U_{dc}^{n}	600 V
Nominal load current	I_{load}^{n}	16.2 A

GCC, grid-connected converter.

The system in the synchronous frame is described by the following differential equations (Choeung et al., 2023; Sreenu et al., 2024):

$$\begin{aligned} v_{\mathrm{d}} &= Ri_{\mathrm{d}} + L\frac{\mathrm{d}i_{\mathrm{d}}}{\mathrm{dt}} - \omega Li_{\mathrm{q}} + v_{\mathrm{d}}^{\mathrm{cnv}}, \\ v_{\mathrm{q}} &= Ri_{\mathrm{q}} + L\frac{\mathrm{d}i_{\mathrm{q}}}{\mathrm{dt}} + \omega Li_{\mathrm{d}} + v_{\mathrm{q}}^{\mathrm{cnv}}, \\ C_{\mathrm{dc}}\frac{\mathrm{d}u_{\mathrm{dc}}}{\mathrm{dt}} &= \frac{3\left(v_{\mathrm{d}}^{\mathrm{cnv}}i_{\mathrm{d}} + v_{\mathrm{q}}^{\mathrm{cnv}}i_{\mathrm{q}}\right)}{2u_{\mathrm{dc}}} - i_{\mathrm{load}}, \end{aligned} \tag{1}$$

where $\omega = 2\pi f_n$ is the pulsatance of grid voltage, $i_{\mathrm{d}}, i_{\mathrm{q}}$ and $v_{\mathrm{d}}, v_{\mathrm{q}}$ are grid current and grid voltage of the dq frame components, respectively, $v_{\mathrm{d}}^{\mathrm{cnv}}, v_{\mathrm{q}}^{\mathrm{cnv}}$ are converter voltage components and u_{dc} is the dc-link voltage.

2.1. Model linearisation

The system described by differential Eq. (1) is non-linear. For design purposes, in order to apply linear system theory for analysis and controller design, we need to linearise the system around a selected operating point. The state-space equations represent the resulting linear system:

$$\dot{x}(t) = Ax(t) + Bu(t) + Ez(t), \tag{2}$$

where $x = \begin{bmatrix} i_{\mathrm{d}} \\ i_{\mathrm{q}} \\ u_{\mathrm{dc}} \end{bmatrix}$ is state vector, $u = \begin{bmatrix} v_{\mathrm{d}}^{\mathrm{cnv}} \\ v_{\mathrm{q}}^{\mathrm{cnv}} \end{bmatrix}$ is input (control) vector and $z = \begin{bmatrix} v_{\mathrm{d}} \\ v_{\mathrm{q}} \\ i_{\mathrm{load}} \end{bmatrix}$ is disturbance vector. The operating

point (x_0, u_0, z_0) is assumed to be the system's nominal condition; thus

$$x_0 = \begin{bmatrix} i_{\mathrm{d0}} \\ i_{\mathrm{q0}} \\ u_{\mathrm{dc0}} \end{bmatrix} = \begin{bmatrix} I_{\mathrm{n}}\sqrt{2} \\ 0 \\ U_{\mathrm{dc}}^{\mathrm{n}} \end{bmatrix}, \; u_0 = \begin{bmatrix} v_{\mathrm{d0}}^{\mathrm{cnv}} \\ v_{\mathrm{q0}}^{\mathrm{cnv}} \end{bmatrix} = \begin{bmatrix} U_{\mathrm{n}}\sqrt{2} - RI_{\mathrm{n}}\sqrt{2} \\ -\omega LI_{\mathrm{n}}\sqrt{2} \end{bmatrix}, \; z_0 = \begin{bmatrix} v_{\mathrm{d0}} \\ v_{\mathrm{q0}} \\ i_{\mathrm{load0}} \end{bmatrix} = \begin{bmatrix} U_{\mathrm{n}}\sqrt{2} \\ 0 \\ I_{\mathrm{load}}^{\mathrm{n}} \end{bmatrix}. \tag{3}$$

To linearise the system around point (x_0, u_0, z_0) we expand $f(x,u,z)$ using a first-order Taylor series:

$$f(x,u,z) \approx f(x_0,u_0,z_0) + \frac{\partial f}{\partial x}\Big|_{(x_0,u_0,z_0)}(x - x_0) + \frac{\partial f}{\partial u}\Big|_{(x_0,u_0,z_0)}(u - u_0) + \frac{\partial f}{\partial z}\Big|_{(x_0,u_0,z_0)}(z - z_0) \tag{4}$$

Since

$$f(x_0,u_0,z_0) = 0 \tag{5}$$

Eq. (4) simplifies to

$$\dot{x} = A\left(x - x_0\right) + B\left(u - u_0\right) + E\left(z - z_0\right), \tag{6}$$

where the Jacobian matrices are defined as:

$$A = \frac{\partial f}{\partial x}|_{(x_0,u_0,z_0)},\ B = \frac{\partial f}{\partial u}|_{(x_0,u_0,z_0)}, E = \frac{\partial f}{\partial z}|_{(x_0,u_0,z_0)}. \tag{7}$$

The general linearisation equation is as follows

$$\delta\dot{x} = \sum\nolimits_i \frac{\partial f}{\partial x_i}\delta x_i + \sum\nolimits_j \frac{\partial f}{\partial u_j}\delta u_j + \sum\nolimits_k \frac{\partial f}{\partial z_k}\delta z_k, \tag{8}$$

Therefore, we have

$$\delta\dot{i}_d = \underbrace{\frac{\partial \dot{i}_d}{\partial i_d}}_{-\frac{R}{L}}\delta i_d + \underbrace{\frac{\partial \dot{i}_d}{\partial i_q}}_{\omega}\delta i_q + \underbrace{\frac{\partial \dot{i}_d}{\partial u_{dc}}}_{0}\delta u_{dc} + \underbrace{\frac{\partial \dot{i}_d}{\partial v_d^{cnv}}}_{-\frac{1}{L}}\delta v_d^{cnv} + \underbrace{\frac{\partial \dot{i}_d}{\partial v_q^{cnv}}}_{0}\delta v_q^{cnv} + \underbrace{\frac{\partial \dot{i}_d}{\partial v_d}}_{\frac{1}{L}}\delta v_d + \underbrace{\frac{\partial \dot{i}_d}{\partial v_q}}_{0}\delta v_q + \underbrace{\frac{\partial \dot{i}_d}{\partial i_{load}}}_{0}\delta i_{load} \tag{9}$$

$$\delta\dot{i}_q = \underbrace{\frac{\partial \dot{i}_q}{\partial i_d}}_{-\omega}\delta i_d + \underbrace{\frac{\partial \dot{i}_q}{\partial i_q}}_{-\frac{R}{L}}\delta i_q + \underbrace{\frac{\partial \dot{i}_q}{\partial u_{dc}}}_{0}\delta u_{dc} + \underbrace{\frac{\partial \dot{i}_q}{\partial v_d^{cnv}}}_{0}\delta v_d^{cnv} + \underbrace{\frac{\partial \dot{i}_q}{\partial v_q^{cnv}}}_{-\frac{1}{L}}\delta v_q^{cnv} + \underbrace{\frac{\partial \dot{i}_q}{\partial v_d}}_{0}\delta v_d + \underbrace{\frac{\partial \dot{i}_q}{\partial v_q}}_{\frac{1}{L}}\delta v_q + \underbrace{\frac{\partial \dot{i}_q}{\partial i_{load}}}_{0}\delta i_{load} \tag{10}$$

$$\delta\dot{v}_{dc} = \underbrace{\frac{\partial \dot{v}_{dc}}{\partial i_d}}_{\frac{3v_{d0}^{cnv}}{2C_{dc}v_{dc0}}}\delta i_d + \underbrace{\frac{\partial \dot{v}_{dc}}{\partial i_q}}_{\frac{3v_{q0}^{cnv}}{2C_{dc}v_{dc0}}}\delta i_q + \underbrace{\frac{\partial \dot{v}_{dc}}{\partial u_{dc}}}_{-\frac{i_{load0}}{C_{dc}v_{dc0}}}\delta u_{dc} + \underbrace{\frac{\partial \dot{v}_{dc}}{\partial v_d^{cnv}}}_{\frac{3i_{d0}}{2C_{dc}v_{dc0}}}\delta v_d^{cnv} + \underbrace{\frac{\partial \dot{v}_{dc}}{\partial v_q^{cnv}}}_{\frac{3i_{q0}}{2C_{dc}v_{dc0}}}\delta v_q^{cnv} + \underbrace{\frac{\partial \dot{v}_{dc}}{\partial v_d}}_{0}\delta v_d + \underbrace{\frac{\partial \dot{v}_{dc}}{\partial v_q}}_{0}\delta v_q + \underbrace{\frac{\partial \dot{v}_{dc}}{\partial i_{load}}}_{-\frac{1}{C_{dc}}}\delta i_{load} \tag{11}$$

Based on Eq. (9)–(11) it can be determined:

$$A = \begin{bmatrix} -\frac{R}{L} & \omega & 0 \\ -\omega & -\frac{R}{L} & 0 \\ \frac{3v_{d0}^{cnv}}{2C_{dc}u_{dc0}} & \frac{3v_{q0}^{cnv}}{2C_{dc}u_{dc0}} & -\frac{i_{load0}}{C_{dc}u_{dc0}} \end{bmatrix},\ B = \begin{bmatrix} -\frac{1}{L} & 0 \\ 0 & -\frac{1}{L} \\ \frac{3i_{d0}}{2C_{dc}u_{dc0}} & \frac{3i_{q0}}{2C_{dc}u_{dc0}} \end{bmatrix},\ E = \begin{bmatrix} \frac{1}{L} & 0 & 0 \\ 0 & \frac{1}{L} & 0 \\ 0 & 0 & -\frac{1}{C_{dc}} \end{bmatrix} \tag{12}$$

Since the linearisation point refers to the equilibrium point, and

$$-Ax_0 - Bu_0 - Ez_0 = 0, \tag{13}$$

we finally obtain from Eq. (6) the model description as in Eq. (2) and matrices like those presented in Eq. (12).

Two design approaches will be introduced, each differing for each version of the control structure. Since the Kessler criteria, which relate to the continuous-domain descriptions of the controller and the object, are used for the design of PI controllers, the control system will be designed in the continuous domain. Subsequently, the controllers will be discretised using a bilinear transform for implementation. This method offers a more accurate phase response than the Euler method. The full-state feedback controller will be designed in the discrete–time domain by representing the control object with a discrete-time equivalent that maintains the step input response.

2.2. Controller and modulator delay

The design of the cascade control system is carried out in the continuous-time domain, while its practical implementation is realised in discrete–time domain. This transition introduces certain considerations that must be addressed during plant modelling. First, the digital implementation of the controller involves fixed-step sampling of the feedback signals, and subsequently, the digital controller computes the control signals, which are generated

with a delay of one sampling step T_s. Second, in the next stage, the control signals are fed to the modulator, which converts them to the continuous domain using the Zero-Order Hold (ZOH) method, introducing an additional delay of half a sampling step. This means that a $1.5T_s$ delay should be included in the system description. The transfer function

$$G_{\text{delay}} = \frac{1}{1.5T_s s + 1} \tag{14}$$

is an approximation of the delay occurring in the inner control loop.

The plant discretisation required for the state controller design is carried out according to the following relations:

$$\begin{cases} x(k+1) = F_1 x(k) + G_1 u(k) + E_1 z(k) \\ y_1(k) = x(k) \end{cases} \tag{15}$$

$$F_1 = \mathrm{e}^{AT_s}, \; [G_1 \; E_1] = A^{-1}(\mathrm{e}^{AT_s} - I)[B \; E] \tag{16}$$

This method already covers the above-mentioned effect of $0.5T_s$ delay, so now the plant description should be extended by a unit delay as follows:

$$\begin{cases} x_2(k+1) = F_2 x(k) + G_2 u_2(k) + E_2 z(k), \\ y_2(k) = x_2(k) \end{cases}$$

$$F_2 = \begin{bmatrix} F_1 & G_1 \\ 0 & 0 \end{bmatrix}, \; G_2 = \begin{bmatrix} 0 \\ I \end{bmatrix}, \; E_2 = \begin{bmatrix} E_1 \\ 0 \end{bmatrix} \tag{17}$$

$$x_2 = \begin{bmatrix} x \\ v_{\text{d}}^{\text{cnv}} \\ v_{\text{q}}^{\text{cnv}} \end{bmatrix}, \; u_2 = \begin{bmatrix} u_{\text{d}} \\ u_{\text{q}} \end{bmatrix},$$

where $u_{\text{d}}, u_{\text{q}}$ are the control signals representing commended converter output voltage components in the d-q frame.

3. Control System Design

3.1. Cascade control structure using PI controllers

A block diagram of a cascade control system with PI controllers is shown in Figure 2. The design of the particular components of this structure is discussed in this section. The current control loop should be designed first. For this purpose, we adopt a simplified description of the control object, assuming a constant voltage u_{dc}. Such a system is described as follows:

$$\begin{cases} \dot{x}_{\text{i}}(t) = A_{\text{i}} x_{\text{i}}(t) + B_{\text{i}} u(t), \\ y_{\text{i}}(k) = x_{\text{i}}(k) \end{cases} \tag{18}$$

$$x_{\text{i}} = x(1{:}2), \; A_{\text{i}} = A(1{:}2,1{:}2), \; B_{\text{i}} = B(1{:}2,1{:}2).$$

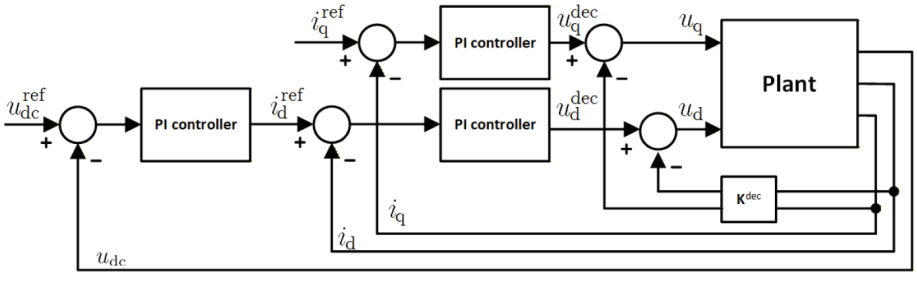

Figure 2. Block diagram of a cascade control structure with PI controllers.

A good practice when designing PI controllers for GCC is to first use feedback decoupling, which allows separating the control paths in the d-q axes, so that each current controller in the d and q axes is not responsible for damping changes resulting from current changes in the other axis.

Feedback decoupling modifies the input as:

$$u = u^{\mathrm{dec}} + K^{\mathrm{dec}} x_{\mathrm{i}}, \tag{19}$$

where $K^{\mathrm{dec}} = \begin{bmatrix} 0 & \omega L \\ -\omega L & 0 \end{bmatrix}$.

The new state matrix is as follows

$$A_i^{\mathrm{dec}} = A_{\mathrm{i}} + B_{\mathrm{i}} K^{\mathrm{dec}} = \begin{bmatrix} -\frac{R}{L} & 0 \\ 0 & -\frac{R}{L} \end{bmatrix} \tag{20}$$

The plant for the current controller is described as follows:

$$\begin{aligned} \dot{x}_i(k) &= A_i^{dec} x_i(k) + B_i u^{dec}(k), \\ y_i(k) &= x_i(k) \end{aligned} \tag{21}$$

Now, the relation between input and output in each d and q axis is described by transfer function

$$G_{\mathrm{I}}(s) = \frac{i_d(s)}{u_d^{cnv}(s)} = \frac{i_q(s)}{u_d^{cnv}(s)} = -\frac{1}{sL + R} \tag{22}$$

Taking into account the delay occurring in the current control loop (Eq. [14]), eventually, the plant for the current controller design purpose is as follows:

$$G_{\mathrm{O}}^{\mathrm{i}}(s) = G_{\mathrm{delay}}(s)\ G_{\mathrm{I}}(s) = \frac{-\frac{1}{R}}{(1.5T_{\mathrm{s}}s + 1)\left(\frac{\mathrm{L}}{R}s + 1\right)}. \tag{23}$$

The PI controller is described as follows:

$$G_{\mathrm{PI}}(s) = K_{PI}\left(1 + \frac{1}{T_i s}\right) = \frac{T_i s + K_{PI}}{T_i s} \tag{24}$$

Current controller parameters $K_{\mathrm{PI}}^{\mathrm{i}}$, $T_{\mathrm{i}}^{\mathrm{i}}$ for the $G_{\mathrm{O}}^{\mathrm{i}}$ object should be designed to achieve a fast and well-damped response; thus, the Modulus Optimum criterion (Galecki and Kaszewski, 2025b; Rabie et al., 2021) is applied as follows:

$$T_{\mathrm{i}}^{\mathrm{i}} = \frac{L}{R},\ K_{\mathrm{PI}}^{\mathrm{i}} = -\frac{L}{3T_{\mathrm{s}}}. \tag{25}$$

For voltage controller design purposes, the current control loop is approximated by a first-order transfer function

$$G_{\mathrm{CL}}^{\mathrm{approx}}(s) = \frac{i_{\mathrm{d}}(s)}{i_{\mathrm{d}}^{\mathrm{ref}}(s)} = \frac{1}{3T_{\mathrm{s}}s + 1} \tag{26}$$

Assuming $i_{\mathrm{d}} = 0$, at the operating point for which linearisation was performed, the relationship between u_{dc} and i_{d} is described by the transfer function:

$$G_2(s)=\frac{u_{\mathrm{dc}}(s)}{i_{\mathrm{d}}(s)}=\frac{A(3,1)}{s-A(3,3)}=\frac{\frac{3v_{\mathrm{d0}}^{\mathrm{cnv}}}{2i_{\mathrm{load0}}}}{\frac{C_{\mathrm{dc}}u_{\mathrm{dc0}}}{i_{\mathrm{load0}}}s+1}=\frac{K_{\mathrm{v}}}{T_{\mathrm{v}}s+1}. \tag{27}$$

The plant for the voltage controller is as follows

$$G_{\mathrm{O}}^{\mathrm{v}}=\frac{u_{\mathrm{dc}}(\mathrm{s})}{i_{\mathrm{d}}^{\mathrm{ref}}}=G_{\mathrm{CL}}^{\mathrm{approx}}G_2(s). \tag{28}$$

For a voltage controller, good disturbance-rejection capabilities are much more important than reference-tracking capabilities; the Symmetrical Optimum criterion is applied (Alrajhi et al., 2025; Rabie et al., 2021). Voltage controller parameters $K_{\mathrm{PI}}^{\mathrm{v}}$, $T_{\mathrm{i}}^{\mathrm{v}}$ for the $G_{\mathrm{O}}^{\mathrm{v}}$ object are set as follows:

$$T_{\mathrm{i}}^{\mathrm{v}}=8T_{\mathrm{s}},\ K_{\mathrm{PI}}^{\mathrm{v}}=-\frac{T_{\mathrm{v}}}{4K_{\mathrm{v}}T_{\mathrm{s}}}. \tag{29}$$

3.2. Full state feedback control structure

A block diagram of a full state feedback control structure is shown in Figure 3. To provide zero steady-state error for constant reference and disturbance signals, and enhance robustness, the control structure, according to the Internal Model Principle (Bin et al., 2022), should include the integrators of control errors $e_{\mathrm{i}}=i_q-i_{\mathrm{q}}^{\mathrm{ref}}$, $e_{\mathrm{v}}=u_{dc}-u_{\mathrm{dc}}^{\mathrm{ref}}$ (Seeber and Tranninger, 2022). For the purposes of designing the feedback gain matrix, this means that two additional state variables augment the object description (Eq. [17]), p_{i} and, p_{v} which represent the states of the integrators mentioned above. In state space representation, this looks as follows:

$$\begin{cases} x_3(k+1)=F_3x_3(k)+G_3u_3(k)+E_3z_3(k), \\ y_3(k)=x_3(k) \end{cases} \tag{30}$$

$$F_3=\begin{bmatrix} & F_2 & & 0 \\ [0_{2\mathrm{x}1} & IT_{\mathrm{s}} & 0_{2\mathrm{x}2}] & I \end{bmatrix},\ G_3=\begin{bmatrix} G_2 \\ 0 \end{bmatrix},\ E_3=\begin{bmatrix} E_2 \\ -I \end{bmatrix},\ x_3=\begin{bmatrix} x_2 \\ p_{\mathrm{i}} \\ p_{\mathrm{v}} \end{bmatrix},\ u_3=u_{2,},\ z_3=\begin{bmatrix} z \\ i_{\mathrm{q}}^{\mathrm{ref}} \\ u_{\mathrm{dc}}^{\mathrm{ref}} \end{bmatrix}.$$

The linear quadratic regulator (LQR) method was used to determine the state controller gain matrix, which optimises the following quality index

$$J=\int_0^{\infty}(x_3^{\mathrm{T}}Qx_3+u_3^{\mathrm{T}}Ru_3), \tag{31}$$

quantifying the total cost of system state deviations and control effort over time. The designer must choose two diagonal matrices, Q and R, keeping in mind that larger Q components result in higher control speed and smaller control errors. In contrast, larger R components result in smoother control and slower response. It is essential to remember that the relative relationship between the Q and R components, rather than their absolute values, is decisive.

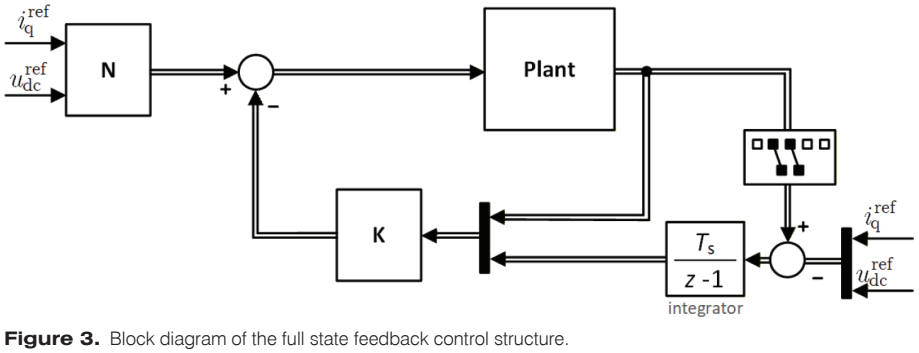

Figure 3. Block diagram of the full state feedback control structure.

For the presented GCC system, tuning was performed using the following steps:

- First, the Bryson correction was applied, normalising the quality index components by scaling each state and control input according to its maximum acceptable value. The Q elements, corresponding to variables p_{i} and p_{v}, were set to 1.
- Next, the penalties for variables i_{q},u_{dc}, and especially p_{i} and, p_{v}, were gradually increased until a satisfactory response time was achieved. Additionally, the penalty for i_{d} was reduced, which also improved the dynamics of the u_{dc} control.
- In the case of excessive oscillations in the impulse response, the penalty coefficients in the R matrix were increased, as well as penalties for $v_{\mathrm{d}}^{\mathrm{cnv}}$ and $v_{\mathrm{q}}^{\mathrm{cnv}}$, as they represent the same physical quantity as the control signals. This and the previous step were performed iteratively until the desired response was achieved.

The following penalty matrices were finally selected:

$$Q = \mathrm{diag}\left(\left[\frac{0.01}{\left(I_{\mathrm{n}}\sqrt{2}\right)^2} \quad \frac{1}{\left(I_{\mathrm{n}}\sqrt{2}\right)^2} \quad \frac{100}{U_{\mathrm{dc}}^{\mathrm{n}\,2}} \quad \frac{10}{(U_{\mathrm{n}}\sqrt{2})^2} \quad \frac{10}{(U_{\mathrm{n}}\sqrt{2})^2} \quad 200 \quad 6000\right]\right),\ R = \mathrm{diag}\left(\left[\frac{10}{(U_{\mathrm{n}}\sqrt{2})^2} \quad \frac{10}{(U_{\mathrm{n}}\sqrt{2})^2}\right]\right). \quad (32)$$

When applying the above steps, the general rule should be remembered that increasing the penalties on state variables i_{d}, i_{q}, u_{dc}, p_{i} and p_{v} at the expense of penalties on the control signal worsens the stability of the changed system, and conversely, larger penalties on control signals increase the stability of the system at the expense of the control dynamics.

3.3. Discussion

Comparing the control structures with PI controllers and the state controller, considering the design challenges and complexity, it must be concluded that neither structure described here offers a significant advantage. Although the design procedure described in Section 2.2 involves a somewhat tedious analytical process that requires describing the control object, (including adopting numerous assumptions) and may pose some difficulties for the designer, it is worth noting that such a precise and analytical selection of PI controller gains is not always necessary. It is presented here as a standard method for tuning PI controllers, ensuring the fairest possible comparison with the state controller in the simulation analysis and highlighting differences arising from the control structure rather than the tuning method itself. In many cases, experienced designers can achieve satisfactory control quality through trial and error, guided by criteria similar to those described in Section 3.2. On the other hand, more complex methods than the one presented here are often used to design a state controller. For example, the pole-placement method requires the engineer to directly locate the poles of a closed-loop system, which requires a good understanding of their impact on the control system's performance and robustness. Therefore, the engineering effort required to tune the controller in the two structures discussed is determined by the design procedure and tools selected by the designer, rather than by the structure itself. In terms of computational complexity, both control structures exhibit very similar requirements. Although the FSF approach involves more multiplications, the PI-based structure requires more integration steps, but these differences are negligible in practice. Modern microcontrollers can execute tens of thousands of such operations within a single sampling period of a discrete-time control system. Typical multiply–accumulate (MAC) operations take on the order of a few nanoseconds (e.g., ~5 ns). Therefore, the computational complexity does not constitute a meaningful differentiating factor between the considered methods in practical applications.

4. Comparative Numerical Analysis of Control Structures

4.1. Simulation result

Both analysed control structures were tested under identical grid-converter operating scenarios. The simulation results are presented in Figures 4 and 5, with Figure 4 showing waveforms in a rotating d-q reference frame and Figure 5 in a stationary reference frame. The waveforms in Figure 4a,b represent the test conditions, grid voltage and load current, respectively. A 15% grid voltage dip occurs from 0.04 s to 0.06 s. A comparison of the response characteristics is presented in Table 2.

The waveforms in Figure 4c,d compare the system response with different control systems. Both systems maintain similar settling times. However, the response characteristics differ significantly. The transient DC voltage dip during

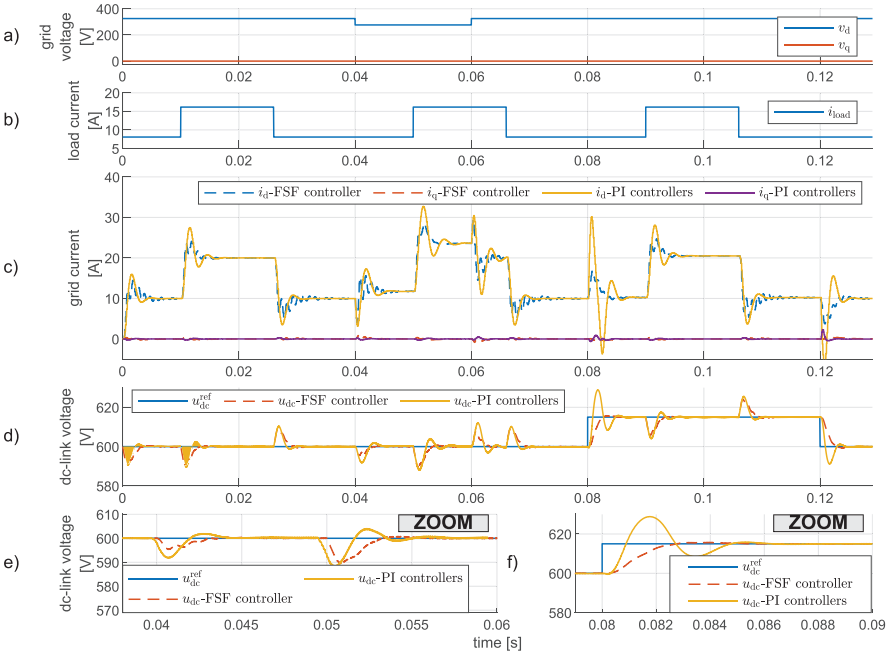

Figure 4. Numerical simulation comparison of the considered control systems represented in synchronous frame: a) grid voltage, b) load current, c) grid current, d) dc-link voltage e) and f) zoom on dc-link voltage.

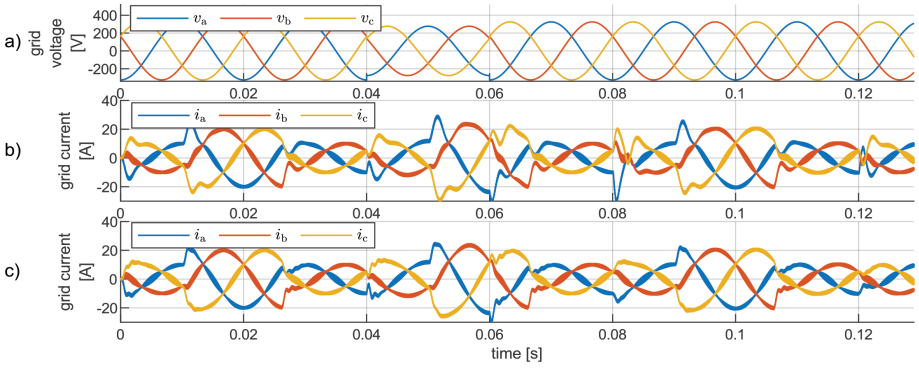

Figure 5. Simulation results illustrating in the stationary frame the performance differences between the two control strategies: a) grid voltage, b) grid current – PI-controller-based cascade structure, c) grid current – FSF control structure.

Table 2. Comparison of the control properties of PI-controller-based and FSF control structures

Performance metric	Cascade PI control	FSF control
Settling time	Fast	Fast
Voltage sag – disturbance rejection	Effective	Highly effective
Step load – disturbance rejection	Effective, moderate oscillations	Effective, well-dumped response
Reference step response	High DC voltage overshoot, High peak current, oscillatory response	Low DC voltage overshoot, moderate peak current, well-dumped response

step changes in load current, for example, at 0.05 s (Figure 4e), is comparable, but the instantaneous current values and the amplitudes of the DC voltage and grid current oscillations are significantly greater for the cascade control system. In the transient state, the peak current value in cascade PI control is 17% higher than in FSF control, with an root mean square (RMS) difference of less than 1%. The standard deviation of v_{dc} from the reference value is also 9% higher. Because the v_{dc} response parameters are similar, the advantage of the FSF system should be noted, given its

lower control cost due to lower peak current. At 0.04 s (Figure 4c) and 0.06 s, we observe the system's response to changes in the grid voltage. The standard deviation of v_{dc} for FSF is 59% lower than for cascade PI control. At time 0.08 s (Figure 4f), a step change in the reference value occurs. Overshoot is 92% and 5% for cascade PI control and FSF control, respectively. The RMS value of the transient current compared to the steady-state value is 7.1 A higher for the PI controllers and only 2.3 A higher for the FSF controller. Therefore, although this is not equally evident in every type of system disturbance, it should be noted that the FSF performs significantly better in this comparison.

Both control structures employ the same dynamic elements, specifically integrating components in the control loops. According to the Internal Model Principle, both control strategies can ensure zero steady-state error and are expected to achieve equivalent steady-state current quality.

4.2. Stability analysis

This section compares the stability of both control structures, highlighting their respective advantages and potential limitations. The assessment was based on the disk margin (DM)'s stability. If the disturbance to which the analysed system is subjected is represented as a complex number, such that its polar coordinates in the complex plane describe the change in amplitude gain and the phase shift, respectively (the point 1 + j0 corresponds to the absence of disturbances), then in this complex plane, the region of disturbances for which the system maintains stability can be determined.

The stability margin, defined as the DM, is the largest radius of the disk entirely contained within the region of disturbances that do not cause the system to lose stability. The graphical meaning is illustrated in the general example in Figure 6. Classic stability margins define the margin only for a single type of disturbance, i.e., exclusively phase or exclusively amplitude. In Figure 6a, the classical stability margins (P_M, G_M) correspond to the furthest point on the x-axis and the point on the unit circle with the largest phase angle for which the system maintains stability. DM is a more conservative approach because, unlike classical stability margins, it defines a stability margin (G_{DM}, P_{DM}) for simultaneous phase and amplitude perturbations. Since DM considers multiplicative perturbations, the amplitude and phase margin defined by DM is smaller than the classical one. The values G_{DM} and P_{DM} mean that at least these perturbation values are guaranteed, even with simultaneous amplitude and phase changes.

Moreover, DM analysis can be performed for simultaneous disturbances in the objects' input and output signals (Figure 6b), further increasing the analysis's conservativeness. Another aspect that makes the DM assessment more reliable is that, for multiple-input multiple-output (MIMO) objects, multi-loop DM analysis assumes the presence of all disturbances across all control paths simultaneously, rather than a single selected control loop.

Table 3 shows the comparative stability results for the two control structures. A graphical depiction of the stability margins is displayed in Figure 7. The control system with the FSF exhibits a considerably greater stability margin, which is a key advantage of the state feedback approach, providing enhanced stability under simultaneous amplitude and phase disturbances. This substantial difference strongly supports the advantages of the state controller. The results clearly indicate that the improved control efficiency discussed in Section 4.2 was not achieved through the reckless selection of controller settings that ignored stability. Additionally, attempting to enhance the system's performance with PI controllers to match the FSF controller, for instance, in terms of disturbance rejection, would lead to an even greater reduction in stability margins.

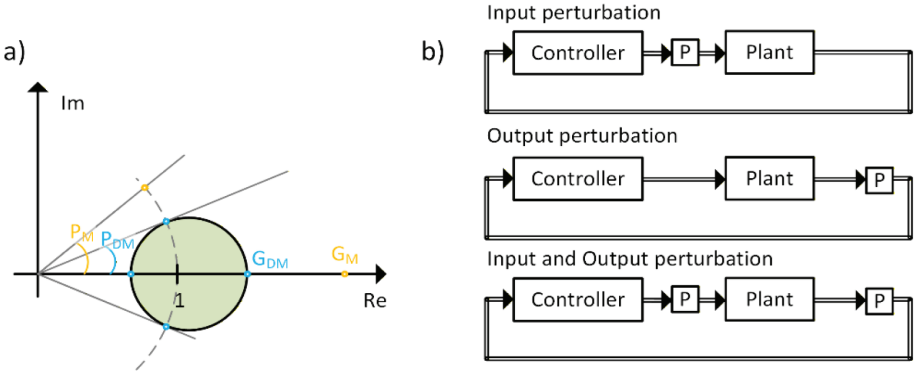

Figure 6. Simulation results illustrating in the stationary frame the performance differences between the two control strategies: a) grid voltage, b) grid current – PI controller based cascade structure, c) grid current – FSF control structure.

4.3. Robustness analysis

Another feature that every high-quality control system should demonstrate is its resistance to changes in model parameters. Figure 8 shows how the system's stability margin changes with changes in the DC link capacitance and input filter inductance. A range of changes from −50% to +100% of the nominal value was analysed. The analysis clearly indicates that the system with the state feedback controller has significantly higher tolerance to parameter variations, representing a major advantage in terms of robustness. In contrast, the PI-based system exhibits a drop in the DM to zero under the same parameter variations, indicating a loss of stability. This highlights a limitation of the PI approach in handling model uncertainties. The nature of changes in stability margins as a function of passive component values is the same for both control structures. The dependence on C_{dc} is monotonic – the smaller the DC capacitance, the smaller the stability margin. However, for changes in input inductance, both control systems achieve maximum stability at approximately 0.77% of the nominal inductance.

5. Final Discussion

In the previous chapters, two control methods were compared comprehensively, each exhibiting specific advantages and disadvantages that influence the choice of control architecture. However, in addition to qualitative comparisons, another feature of the control system should be mentioned, as it may also influence the choice of control architecture designers. Such a feature is the ability to modify the designed linear control system to limit the inductor current and the control signal.

Table 3. DM based stability analysis results

Performance metric		DMs at plant inputs	DMs at plant outputs	DM at both inputs and outputs
Cascade PI control	Disk size	0.4245	0.1827	0.1311
	Gain margin	[0.6499 1.5388]	[0.8326 1.2010]	[0.8770 1.1402]
	Phase margin	[−23.9640 23.9640]	[−10.4367 10.4367]	[−7.4982 7.4982]
FSF control	Disk size	0.8196	0.2175	0.1822
	Gain margin	[0.4186 2.3887]	[0.8038 1.2440]	[0.8330 1.2004]
	Phase margin	[−44.5681 44.5681]	[−12.4128 12.4128]	[−10.4088 10.4088]

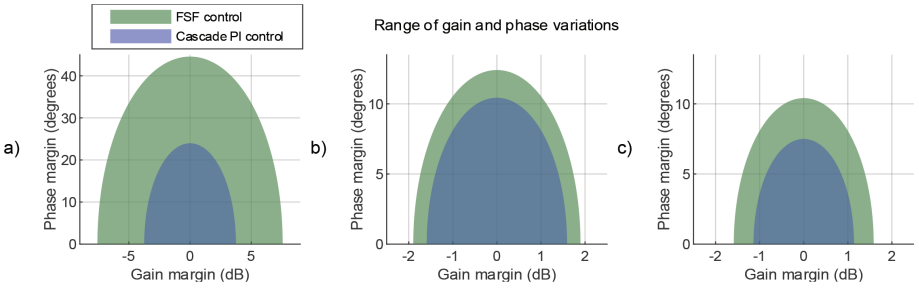

Figure 7. Disk-based stability margins of the control system for a) input perturbation, b) output perturbation, c) simultaneous input and output perturbation.

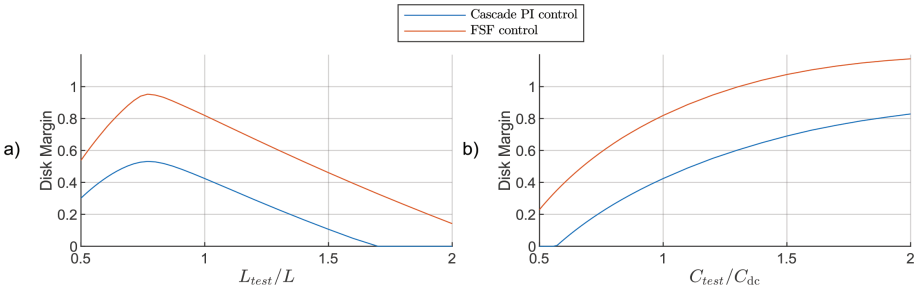

Figure 8. Effect of input filter inductance (a) and DC-link capacitance (b) variations on the stability margin.

In the case of a cascade PI control system, implementing constraints is straightforward, which is an advantage. It involves saturating the output signals of PI controllers and implementing an anti-windup mechanism.

It may seem that effective current limiting in the FSF controller is impossible or very demanding, because the control structure (Figure 3) does not include the $i_{\mathrm{d}}^{\mathrm{ref}}$, signal or any other signal linearly dependent on the setpoint value of the current component $i_{\mathrm{d}}^{\mathrm{ref}}$, so direct manipulation of the current value is not possible. However, this problem is very effectively and simply addressed by the multithreaded state control mechanism, first proposed in Michalczuk et al. (2021). This technique was later successfully implemented in the permanent magnet synchronous motor (PMSM) drive (Harikrishnan and Arun Rahul, 2024) and GCC (Michalczuk et al., 2024). Implementing additional state feedback paths and a simple mechanism for selecting the current control signal permits low implementation effort to introduce constraints into the FSF controller system while retaining all of its control-quality advantages.

In summary, the cascade PI method is simple, easy to implement and allows straightforward constraint handling, but may require careful loop tuning. The FSF method offers higher control performance and effective decoupling, and, with the mentioned multithreaded strategy, constraint implementation can be achieved effectively with low effort.

6. Conclusions

This paper examines two methods for controlling a GCC. It compares a cascade control structure that utilises PI controllers with a full-state feedback control structure. Both control strategies were designed using the same plant model, operating point and delay assumptions, enabling the observed differences to be mainly attributed to the control architecture rather than the tuning methodology. The comparative simulation results show that both control systems offer rapid dynamic responses and stable operation under nominal conditions. However, the full-state feedback controller consistently delivers superior transient performance, particularly in terms of lower peak currents, reduced oscillations in the DC-link voltage and significantly smaller overshoot during reference changes. These benefits are particularly important in practical applications, where current limits and component stress are key design considerations.

The stability analysis based on DMs demonstrated that the full-state feedback control structure provides significantly greater stability margins than the cascaded PI control system. This confirms that the enhanced dynamic performance of the state controller is achieved without sacrificing robustness. Conversely, robustness analysis of passive component variations further revealed that the state-feedback-based system can tolerate larger parameter uncertainties without losing stability.

The findings of this research offer compelling reasons in favour of full-state feedback control for GCCs, especially in applications requiring high robustness and strict dynamic performance.

Acknowledgements

The research was supported by the Institute of Control and Industrial Electronics, Faculty of Electrical Engineering, Warsaw University of Technology, Warsaw, Poland, within its subsidy funds.

References

Alrajhi, H., Al-Harbi, Y., Al-Zahrani, A., Raza, S. A., Daraz, A. and Al-Kaabi, M. (2025). Comprehensive Analysis of PI Tuning Techniques for VSC Applications. *Journal of Umm Al-Qura University for Engineering and Architecture*, 16(3), pp. 599–616. doi: 10.1007/s43995-025-00139-8

Åström, K. J. and Murray, R. (2021). *Feedback Systems: An Introduction for Scientists and Engineers*. Princeton: Princeton University Press.

Bin, M., Astolfi, D. and Marconi, L. (2022). About Robustness of Control Systems Embedding an Internal Model. *IEEE Transactions on Automatic Control*, 68(3), pp. 1306–1320. doi: 10.1109/TAC.2022.3151574

Busada, C. A., Jorge, S. G. and Solsona, J. A. (2015). Full-State Feedback Equivalent Controller for Active Damping in LCL-Filtered Grid-Connected Inverters Using a Reduced Number of Sensors. *IEEE Transactions on Industrial Electronics*, 62(10), pp. 5993–6002. doi: 10.1109/TIE.2015.2424391

Choeung, C., Tang, H., Soth, P., Keo, S., Leang, P., Cheng, H., Srang, S. and Huy, V., 2023. Linear matrix inequality-based optimal state feedback control of a three-phase L-filtered grid-connected

inverter. In: *2023 Third International Symposium on Instrumentation, Control, Artificial Intelligence, and Robotics (ICA-SYMP)*.

Dmitruk, K. (2024). A Simplified Guide to Control Algorithms for Grid Converters in Renewable Energy Systems. *Energies*, 17(18), p. 4690. doi: 10.3390/en17184690

Franklin, G. F., Powell, J. D., Emami-Naeini, A. and Powell, J. D. (2002). *Feedback Control of Dynamic Systems*. Upper Saddle River: Prentice hall.

Galecki, A. and Kaszewski, A. (2025a). Current control of a grid-connected converter with an LCL filter using small-signal analysis considering grid impedance. In: *2025 Progress in Applied Electrical Engineering PAEE*, IEEE, pp. 1–6.

Galecki, A. and Kaszewski, A. (2025b). Impact of Grid Impedance on Current Control in Grid-Connected Converters with LCL Filters. *Przegląd Elektrotechniczny*, 11, pp. 257–266, doi: 10.15199/48.2025.11.37

Guo, X. Q., Wu, W. Y. and Gu, H. R. (2011). Phase Locked Loop and Synchronization Methods for Grid-Interfaced Converters: A Review. *Przegląd Elektrotechniczny*, 87(4), pp. 182–187.

Harikrishnan, S. and Arun Rahul S. (2024). State feedback speed control of PMSM using multithreaded controller. In *2024 IEEE International Conference on Power Electronics, Drives and Energy Systems PEDES*, IEEE: Jaipur, India, (pp. 1–6).

Iwański, G., Chustecki, P. and Gałecki, A. (2023). Właściwości przekształtnika sieciowego z filtrem LCL ze sprzęże-niem od wspólnego pomiaru prądów cewek filtru. *Przeglad Elektrotechniczny*, 99(3), pp. 30–35, doi:10.15199/48.2023.03.05.

Iwanski, G., Luszczyk, T. and Szypulski, M. (2016). Virtual-Torque-Based Control of Three-Phase Rectifier Under Grid Imbalance and Harmonics. *IEEE Transactions on Power Electronics*, 32(9), pp. 6836–6852. doi: 10.1109/TPEL.2016.2626638

Iwanski, G., Wodyk, S. and Luszczyk, T. (2021). Control of a Three-Phase Power Converter Connected to Unbalanced Power Grid in a Non-Cartesian Oblique Frame. *IEEE Transactions on Power Electronics*, 37(1), pp. 183–195. doi: 10.1109/TPEL.2021.3098697

Iwaszkiewicz, J., Mysiak, P. and Muc, A. (2025). Current Controlled AC/DC Converter and Its Performance—A Mathematical Model. *Energies*, 18(2), p. 419. doi: 10.3390/en18020419

Krystkowiak, M. and Gwóźdź, M. (2018). Power Electronics Converter for PV Pannel Working With a Power Grid. *Power Electronics and Drives*, 35.

Krystkowiak, M., and Gwóźdź, M. (2015). Power Electronics Converter for PV Pannel Working With a Power Grid. *Power Electronics and Drives*, 35, pp. 40–51.

Kulikowski, K. and Sikorski, A. (2016). New DPC Look-up Table Methods for Three-Level AC/DC Converter. *IEEE Transactions on Industrial Electronics*, 63(12), pp. 7930–7938. doi: 10.1109/TIE.2016.2538208

Liu, B., Xiang, X., Yang, H., Li, W. and He, X. (2025). Fault Inrush Current Characterization of Grid Forming Converter Based on Analytical Calculation. *IEEE Transactions on Industrial Electronics*, 73(3), pp. 5013–5018, doi: 10.1109/TIE.2025.3607993.

Michalczuk, M., Galecki, A., Ufnalski, B., Jackiewicz, K. and Kaszewski, A. (2023). Stability-Assured Design of a Full State Feedback Controller for a Three-Phase Grid-Connected Converter Using Disk Margin Analysis. *ISA Transactions*, 140, pp. 459–471. doi: 10.1016/j.isatra.2023.06.007

Michalczuk, M., Ufnalski, B. and Gałecki, A. (2024). Multithreaded State Controller for Grid-Connected Converter With Imposed Limits. *IEEE Transactions on Industrial Electronics*, 71(4), pp. 4006–4015. doi: 10.1109/TIE.2023.3279553

Michalczuk, M., Ufnalski, B. and Grzesiak, L. M. (2021). Imposing Constraints in a Full State Feedback System Using Multithreaded Controller. *IEEE Transactions on Industrial Electronics*, 68(12), pp. 12543–12553. doi: 10.1109/TIE.2020.3044778

Peykarporsan, R., Oshnoei, S., Fathollahi, A. and Lie, T. T. (2025). A Novel Intelligent Fractional Order Cascade Control to Enhance Wind Energy Conversion in Wind Farms: A Practical Case Study. *IEEE Transactions on Energy Conversion*, 40(3), pp. 1736–1749. doi: 10.1109/TEC.2025.3543144

Piasecki, S., Jasiński, M., Wrona, G. and Chmielak, W. (2012). Robust control of grid connected AC-DC converter for distributed generation. In: *IECON 2012-38th Annual Conference on IEEE Industrial Electronics Society*, IEEE: Montreal, Canada, (pp. 5840–5845).

Rabie, D., Senjyu, T., Alkhalaf, S., Mohamed, Y. S. and Shehata, E. G. (2021). Study and Analysis of Voltage Source Converter Control Stability for HVDC System Using Different Control Techniques. *Ain Shams Engineering Journal*, 12(3), pp. 2763–2779. doi: 10.1016/j.asej.2020.12.013

Rahman, F. M., Kukkola, J., Pirsto, V., Routimo, M., and Hinkkanen, M. (2020). Observers for discrete-time current control of converters equipped with an LCL filter. In: *2020 IEEE Energy Conversion Congress*

and Exposition (ECCE), IEEE: Detroit, Michigan, USA, pp. 2884–2891.

Seeber, R. and Tranninger, M. (2022). Integral State-Feedback Control of Linear Time-Varying Systems: A Performance Preserving Approach. *Automatica*, 136, p. 110000. doi: 10.1016/j.automatica.2021.110000

Sreenu, C., Mallesham, G., Chandra Shekar, T. and Salkuti, S. R. (2024). Pairing Voltage-Source Converters with PI Tuning Controller Based on PSO for Grid-Connected Wind-Solar Cogeneration. *Franklin Open*, 8, p. 100138. doi: 10.1016/j.fraope.2024.100138

Sun, Y., Ruan, X., He, Y., Lin, Z. and Yan, Y. (2026). Symmetrical Phase-Locked Loop and Power Control Loop for Grid-Connected Inverters. *IEEE Transactions on Power Electronics*, 41(6), pp. 9787–9798. doi: 10.1109/TPEL.2025.3648877

Tian, Y., Wang, Y., An, L. and Yue, Z. (2025a). Full-State Feedback Control for Grid-Connected DC/AC Converter with Enhanced Stability and Controllability. *IEEE Transactions on Industrial Electronics*, 72(8), pp. 8017-8027. doi: 10.1109/TIE.2024.3525100.

Tian, Y., Xu, X., Wang, Y., Li, Z., Zhang, Z. and Gao, Y. (2025b). Full-State Feedback Power Decoupling Control for Grid Forming Converter With Improved Stability and Inertia Response. *IEEE Transactions on Power Electronics*, 40(2), pp. 2930–2942. doi: 10.1109/TPEL.2024.3487620

Ufnalski, B., Michalczuk, M. and Galecki, A. (2022). Robust Tuning of Multiresonant Current Controllers for Grid-Tied Converters and Erroneous Use of the Naslin Polynomial Method. *IEEE Access*, 10, pp. 88211–88225. doi: 10.1109/ACCESS.2022.3199702

Zhao, J., Huang, M., Yan, H., Tse, C. K. and Zha, X. (2021). Nonlinear and Transient Stability Analysis of Phase-Locked Loops in Grid-Connected Converters. *IEEE Transactions on Power Electronics*, 36(1), pp. 1018–1029. doi: 10.1109/TPEL.2020.3000516